ROYAL SOCIETY OF CHEMISTRY

PAPER

Check for updates

Organic–inorganic hybrids assembled from plenary Keggin-type germanotungstate units and 3d–4f heterometal clusters†

Huijie Li,[a] Peijun Gong,[a] Jun Jiang,[a] Yamin Li,[a] Jingjing Pang,[a] Lijuan Chen*[a] and Junwei Zhao [ID] *[a,b]

Two kinds of organic–inorganic 3d–4f heterometal hybrids based on plenary α-Keggin-type germano-tungstates $[Cu_2(H_2O)_3(PA)_3]$ $[Ln_{0.5}Na_{0.5}Cu_2(H_2O)_{12}(PA)_3][\alpha\text{-}GeW_{12}O_{40}]\cdot5H_2O$ [Ln = La^{3+} (**1**), Ce^{3+} (**2**)] and $[Cu_2(H_2O)_2(PA)_3][Cu(PA)_2][Ln(H_2O)_7][\alpha\text{-}GeW_{12}O_{40}]\cdot7H_2O$ [Ln = Tb^{3+} (**3**), Dy^{3+} (**4**), HPA = 2-picolinic acid] were prepared *via* the strategy of combining an *in situ* assembly reaction and stepwise synthesis in the aqueous solution. The most remarkable structural characteristic of **1–2** is that neighboring structural units are connected into a 1-D chain alignment by the bridging di-copper $[Cu_2(H_2O)_3(PA)_3]^+$ subunits, whereas the most outstanding structural feature of **3–4** is that neighboring structural units are interconnected to generate a zigzag 1-D chain alignment by the bimetallic bridging $[Cu_2(H_2O)_3(PA)_3]^+$ subunits, and then adjacent zigzag 1-D chains are integrated into a fascinating 2-D sheet structure by heterobimetallic bridging $\{Tb(H_2O)_7[Cu(PA)_2]_{0.5}\}^{3+}$ subunits and $[Cu(PA)_2]$ groups. As far as we know, **1–4** represent the first examples of plenary Keggin heterometal germanotungstates including organic 3d–4f heterometal subunits so far. The electrochemical sensing properties towards the detection of Acetaminophen of **1/3**@CMWCNT–Nafion/GCE electrochemical sensors were investigated, showing that **1/3**@CMWCNT–Nafion/GCE electrochemical sensors exhibit good stability and good sensing performance towards AC detection.

Introduction

Polyoxometalates (POMs) are early transition-metal oxide anionic clusters with high oxidation states (including Mo^{VI}, W^{VI}, V^V, Nb^V and Ta^{IV}), which exhibit unrivalled structural diversities, charming properties and underling applications in catalysis, magnetism, medicine, materials science and nano-technology.[1] What's more, POMs can serve as functional in-organic nucleophilic polydentate ligands to incorporate 3d-metal or 4f-metal ions to manufacture novel 3d-metal substituted POM materials or 4f-metal substituted POM materials with potential applications. Therefore, the design and synthesis of 3d- or 4f-metal incorporated POMs have attracted comprehensively increasing interest on account of their appli-

cations in various fields including catalysis, electrochemistry, luminescence, conductivity and magnetic properties.[2] In recent years, developing organic–inorganic hybrid 3d- or 4f-metal incorporated POMs has appealed considerable attraction and great achievements on 3d- or 4f-metal incorporated POMs have been made.[3–4] However, exploring and preparing novel organic–inorganic POM-based hybrids simultaneously contain-ing 3d- and 4f-metal ions is a still challenging field. Thereinto, Keggin-type POMs as good candidates can be used as flexible building blocks to integrate 3d- and 4f-metal ions to construct organic–inorganic hybrid 3d–4f heterometal incorporated POMs (DFHIPs) with complex structures and special properties.[5] In 2008, Liu *et al.* isolated a family of 1-D chain DFHIPs $[\{Ln(PW_{11}O_{39})\}\{Cu_2(bpy)_2(\mu\text{-ox})\}]^{9-}$ (Ln = La^{3+}, Pr^{3+}, Eu^{3+}, Gd^{3+}, Yb^{3+}) with bipyridine-oxalate double ligands.[6] In 2009, Mialane *et al.* discovered three unique heterometal $\{LnCu_3(OH)_3(O(W))\}$-cubane (Ln = La^{3+}, Gd^{3+}, Eu^{3+}) inserted POMs.[7] In 2011, Niu's group reported six DFHIPs with mixed organic ligands based on 1 : 2-type $[Ln(\alpha\text{-}PW_{11}O_{39})_2]^{11-}$ units (Ln = Ce^{3+}, Pr^{3+}, Gd^{3+}, Tb^{3+}, Er^{3+}, Nd^{3+}).[8] In 2013, Yang *et al.* addressed an interesting 3-D organic–inorganic 3d–4f heterometal framework $[Ce_2(ox)_3(H_2O)_2]_2\{[Mn(H_2O)_3]_2[Mn_4(GeW_9O_{34})_2(H_2O)_2]\}^{8-}$ estab-lished by tetra-Mn^{II} sandwiched POMs and mixed Mn^{2+}

[a]Henan Key Laboratory of Polyoxometalate Chemistry, College of Chemistry and Chemical Engineering, Henan University, Kaifeng, Henan 475004, China. E-mail: ljchen@henu.edu.cn, zhaojunwei@henu.edu.cn
[b]State Key Laboratory of Structural Chemistry, Fujian Institute of Research on the Structure of Matter, Chinese Academy of Sciences, Fuzhou, Fujian 350002, China
†Electronic supplementary information (ESI) available: The refinement details and additional figures. CCDC 1891064–1891067. For ESI and crystallographic data in CIF or other electronic format see DOI: 10.1039/c9dt00312f

and Ce^{3+} linkers.[9] In 2014, our group reported the first series of 3d–4f heterometal incorporated tungstoantimonates functionalized by amino acids [Ln(H$_2$O)$_8$]$_2$[Fe$_4$(H$_2$O)$_8$(thr)$_2$] [B-β-SbW$_9$O$_{33}$]$_2$·22H$_2$O (Ln = Pr^{3+}, Nd^{3+}, Sm^{3+}, Eu^{3+}, Gd^{3+}, Dy^{3+}, Lu^{3+}).[10] In 2017, Long and collaborators communicated the anion-dependent assembly of 3d–4f heterometal clusters based on a lacunary POM unit.[11] In 2018, Li *et al.* provided four banana-shaped heterometal {Fe$_6$LnO$_{28}$}-substituted (Ln = Tb^{3+}, Dy^{3+}, Ho^{3+}, Er^{3+}) germanotungstates (GTs).[12]

Apparently, most the previously reported DFHIP hybrids are based on lacunary Keggin-type POMs as the archetypal building blocks. In contrast, to date, there are very few reports on organic–inorganic hybrid DFHIPs containing saturated Keggin-type POM units primarily because the saturated Keggin-type POM units have a low negative charge compared to the lacunary POM units, which makes it considerably difficult for saturated Keggin-type POM units to simultaneously combine 3d- and 4f-metal ions. Thus, this background provides us with an excellent opportunity to explore this challenging field. Recently, we have developed a strategy of combining the *in situ* assembly reaction and stepwise synthesis to prepare organic–inorganic POM-based hybrids. In this work, also, we used this synthetic strategy to explore organic–inorganic hybrid DFHIPs with saturated Keggin-type POM units based on the following considerations: (i) to overcome the main difficulty of saturated Keggin-type POM units having a low negative charge and simultaneously combining 3d- and 4f-metal ions, we can utilize the organic carboxylic acid ligands to solve this obstacle since carboxylic acid ligands can be deprotonated to the carboxylate anions and supplement the low negative charge of saturated Keggin-type POM units in the reaction system; moreover, in this paper, we selected 2-picolinic acid (HPA) as the multifunctional ligand because it not only can supplement the low negative charge of saturated Keggin-type POM units, but also it is a rigid ligand with oxygen and nitrogen donors, which makes it act as a bidentate group to connect 3d- and 4f-metal ions favouring construction of novel organic–inorganic hybrid DFHIPs assembled from mixed 3d–4f heterometal clusters and saturated Keggin-type POM units. (ii) In this work, we chose GeO$_2$ and Na$_2$WO$_4$·2H$_2$O as the starting materials to *in situ* assemble saturated Keggin-type POM units because not only is the facile reaction of GeO$_2$ and Na$_2$WO$_4$·2H$_2$O beneficial to generate the saturated Keggin-type GT polyanions, but also GTs have become an important subfamily of POMs and have developed into a new research focus and a challenging field; moreover, the research on 3d- and 4f-metal incorporated GTs was not largely explored.[13] (iii) Compared with the other 3d-metal cations, electrophilic Cu^{2+} ions exhibit more flexible coordination modes and easily coordinate to the surface oxygen atoms of GT fragments and the nitrogen or oxygen atoms of HPA. Furthermore, the Jahn–Teller effect of the octahedral geometry and the pseudo-Jahn–Teller effect of the square pyramid geometry of Cu^{2+} ions are capable of reducing steric hindrance, which will offer a great possibility for the formation of multi-dimensional materials.[8,14] (iv) The 4f-metal cations are exceptionally versa-

tile structural linkers due to their high coordination numbers, which is beneficial to combine Cu-organic components together and give birth to multi-dimensional DFHIP materials.[15] On the basis of these aforementioned ideas, two kinds of organic–inorganic DFHIP hybrids based on plenary Keggin-type GT polyanions [Cu$_2$(H$_2$O)$_3$(PA)$_3$][Ln$_{0.5}$Na$_{0.5}$Cu$_2$ (H$_2$O)$_{12}$(PA)$_3$][α-GeW$_{12}$O$_{40}$]·5H$_2$O [Ln = La^{3+} (**1**), Ce^{3+} (**2**)] and [Cu$_2$(H$_2$O)$_2$(PA)$_3$][Cu(PA)$_2$]$_{1.5}$[Ln(H$_2$O)$_7$][α-GeW$_{12}$O$_{40}$]·7H$_2$O [Ln = Tb^{3+} (**3**), Dy^{3+} (**4**)] were obtained, delegating the first inorganic–organic hybrid DFHIPs based on plenary Keggin-type GT units. Besides, they were also characterized by elemental analyses, IR spectra, thermogravimetric (TG) analyses and single-crystal X-ray diffraction. The electrochemical sensing properties of **1**/**3**@CMWCNT–Nafion/GCE electrochemical sensors towards the detection of Acetaminophen (AC) were evaluated (CMWCNs = carboxyl functionalized multi-walled carbon nanotubes). Experimental results reveal that **1**/**3**@CMWCNT–Nafion/GCE electrochemical sensors show good stability and low limits of detection (LODs). The LODs of **1**/**3**@CMWCNT–Nafion/GCE electrochemical sensors are 1.07 and 1.08 μmol L^{-1} in a linear concentration range of 10–1000 μmol L^{-1}, which would open new opportunities for POM-based materials serving as biosensors for sensitive detection of biomolecules.

Experimental

Materials and physical measurements

All chemicals were commercially purchased and were of analytical reagent grade and used without further purification. Elemental analyses (C, H and N) were performed on a Perkin–Elmer 2400–II CHNS/O analyzer. The PXRD pattern was collected on a Bruker AXS D8 Advance diffractometer with Cu Kα radiation (λ = 1.54056 Å) in the range of 2θ = 5–50° at 293 K. UV absorption spectra were collected on a U-4100 spectrometer from 200 to 800 nm at room temperature. IR spectra were obtained from solid samples pelletized with KBr on a Nicolet 170 SXFT-IR spectrometer in the range of 400–4000 cm^{-1}. TG analyses were performed under a N$_2$ atmosphere on a Mettler–Toledo TGA/SDTA 851^e instrument between 25 and 1000 °C at a heating rate of 10 °C min^{-1}. Cyclic voltammograms were recorded on a CS electrochemical workstation (Wuhan Corrtest Instrument Co. Ltd) at room temperature. A conventional three-electrode system was used. Platinum gauze was used as a platinum electrode, and a saturated calomel electrode was used as a reference electrode. Chemically bulk-modified glassy carbon electrodes (GCEs) were used as the working electrodes.

Synthesis of [Cu$_2$(H$_2$O)$_3$(PA)$_3$][La$_{0.5}$Na$_{0.5}$Cu$_2$(H$_2$O)$_{12}$(PA)$_3$] [α-GeW$_{12}$O$_{40}$]·5H$_2$O (1)

GeO$_2$ (0.125 g, 1.195 mmol) and Na$_2$WO$_4$·2H$_2$O (1.002 g, 3.032 mmol) were added to 10 mL distilled water under stirring at room temperature. After stirring for 5 min, the pH of the solution was adjusted to 1.10 by using 6 mol L^{-1} HCl solu-

tion. And then the solution was heated in a 60 °C water bath for 30 min, followed by the successive addition of $CuCl_2 \cdot 2H_2O$ (0.200 g, 1.173 mmol), HPA (0.082 g, 0.650 mmol), and La $(NO_3)_3 \cdot 6H_2O$ (0.225 g, 0.519 mmol). The solution was kept in the 60 °C water bath for another 2 hours and then cooled to room temperature. After filtration, the resulting solution was kept at room temperature and mazarine block crystals were obtained after several days and dried in air. Yield: ca. 31% (based on $La(NO_3)_3 \cdot 6H_2O$). Anal. calcd (found%) for $C_{36}H_{64}Cu_4GeLa_{0.5}N_6Na_{0.5}O_{72}W_{12}$(1): C 9.94 (10.15), H 1.48 (1.57), N 1.93 (1.81). IR (KBr, cm^{-1}): 3417 (s), 1619 (m), 1592 (m), 1570 (m), 1484 (m), 1451 (w), 1419 (m), 1397 (m), 1297 (m), 1269 (w), 1057 (w), 974 (s), 882 (m), 833 (m), 787 (m), 749 (m), 694 (s), 532 (w) (Fig. S1†).

Synthesis of $[Cu_2(H_2O)_3(PA)_3][Ce_{0.5}Na_{0.5}Cu_2(H_2O)_{12}(PA)_3]$ $[\alpha\text{-}GeW_{12}O_{40}] \cdot 5H_2O$ (2)

The synthetic procedure of **2** was similar to that of **1** except that $La(NO_3)_3 \cdot 6H_2O$ (0.225 g, 0.517 mmol) was replaced by $Ce(NO_3)_3 \cdot 6H_2O$ (0.225 g, 0.520 mmol). Yield: ca. 30% (based on $Ce(NO_3)_3 \cdot 6H_2O$). Anal. calcd (found%) for $C_{36}H_{64}Cu_4GeCe_{0.5}N_6Na_{0.5}O_{72}W_{12}$ (**2**): C 9.95 (10.19), H 1.48 (1.62), N 1.93 (2.07). IR (KBr, cm^{-1}): 3425 (s), 1618 (m), 1591 (m), 1569 (m), 1480 (m), 1451 (w), 1418 (m), 1397 (m), 1298 (m), 1270 (w), 1056 (w), 972 (s), 887 (m), 829 (m), 785 (m), 755 (m), 697 (s), 536 (w) (Fig. S1†).

Synthesis of $[Cu_2(H_2O)_2(PA)_3][Cu(PA)_2][Tb(H_2O)_7]$ $[\alpha\text{-}GeW_{12}O_{40}] \cdot 7H_2O$ (3)

The synthetic procedure of **3** was similar to that of **1** except that $La(NO_3)_3 \cdot 6H_2O$ (0.225 g, 0.517 mmol) was replaced by $Tb(NO_3)_3 \cdot 6H_2O$ (0.225 g, 0.497 mmol). Yield: ca. 30% (based on $Tb(NO_3)_3 \cdot 6H_2O$). Anal. calcd (found%) for $C_{30}H_{52}Cu_3GeN_5O_{66}TbW_{12}$ (**3**): C 8.65 (8.78), H 1.26 (1.44), N 1.68 (1.53). IR (KBr, cm^{-1}): 3425 (s), 1622 (m), 1592 (m), 1570 (m), 1482 (m), 1452 (w), 1411 (m), 1388 (m), 1365 (m), 1295 (m), 1269 (w), 1053 (w), 969 (s), 887 (m) 834 (m), 787 (m), 758 (m), 694 (s), 537 (w) (Fig. S1†).

Synthesis of $[Cu_2(H_2O)_2(PA)_3][Cu(PA)_2] [Dy(H_2O)_7]$ $[\alpha\text{-}GeW_{12}O_{40}] \cdot 7H_2O$ (4)

The synthetic procedure of **4** was similar to that of **1** except that $La(NO_3)_3 \cdot 6H_2O$ (0.225 g, 0.517 mmol) was replaced by $Dy(NO_3)_3 \cdot 6H_2O$ (0.225 g, 0.492 mmol). Yield: ca. 28% (based on $Dy(NO_3)_3 \cdot 6H_2O$). Anal. calcd (found%) for $C_{30}H_{52}Cu_3DyGeN_5O_{66}W_{12}$ (**4**): C 8.64 (8.79), H 1.26 (1.39), N 1.68 (1.49). IR (KBr, cm^{-1}): 3419 (s), 1622 (m), 1593 (m), 1571 (m), 1481 (m), 1452 (w), 1411 (m), 1388 (m), 1366 (m), 1298 (m), 1269 (w), 1057 (w), 969 (s), 887 (m), 834 (m), 781 (m), 758 (m), 694 (s), 534 (w) (Fig. S1†).

Preparation of 1/3@CMWCNT–Nafion/GCE electrochemical sensors

The preparation process of the **1**@CMWCNT–Nafion/GCE electrochemical sensor is as follows: (a) CMWCNTs (10.0 mg) and **1** (9.6 mg) were dispersed in deionized water (1.0 mL) under ultrasonication for 6 h to obtain a homogeneous suspension. (b) The suspension was centrifuged for 20 min at a rate of 12 000 r min^{-1}, the clear liquid was poured out and then highly purified water (1.0 mL) was added to wash precipitates under ultrasonication for 20 min and precipitates were washed three times in the same way. (c) After the third time of washing precipitates, highly purified water (1.0 mL) and Nafion (20.0 μL) were added to precipitates. After ultrasonication for 20 min, the resulting suspension (10.0 μL) was dropped onto the surface of the polished GCE. (d) In order to consolidate the film on the GCE, the resulting suspension from step c was dispersed under ultrasonication for another 20 min before dropping another 10.0 μL onto the same GCE for another time after drying at room temperature in air. Then the **1**@CMWCNT–Nafion/GCE electrochemical sensor was obtained and can be used. The schematic preparation process of the **1**@CMWCNT–Nafion/GCE electrochemical sensor is displayed in Fig. 1. (e) Then, the obtained **1**@CMWCNT–Nafion/ GCE electrochemical sensor should be activated in 0.1 mol L^{-1} NaH_2PO_4–Na_2HPO_4 buffer solution in the potential range of −1.3–1.0 V at a scan rate of 100 mV s^{-1} until getting stable response current and then washed with water before use. The preparation process of the **3**@CMWCNT–Nafion/GCE electrochemical sensor is the same as that of the **1**@CMWCNT– Nafion/GCE electrochemical sensor.

Then other stock solutions were prepared. First, AC was dissolved in ethanol to prepare two kinds of AC solutions with a concentration of 0.1 mol L^{-1} and 0.01 mol L^{-1}, respectively. Second, 0.1 mol L^{-1} NaH_2PO_4–Na_2HPO_4 buffer solution was prepared by dissolving 7.800 g $NaH_2PO_4 \cdot 2H_2O$ and 17.907 g $Na_2HPO_4 \cdot 12H_2O$ in the deionized water to obtain 500 mL buffer solution, and the target pH value was adjusted by using concentrated phosphoric acid or 2 mol L^{-1} NaOH solution. Of course, all the solutions were prepared with highly purified water. All the electrochemical measurements were carried out on an electrochemical workstation with a conventional three-electrode system.

X-ray crystallography

The good-quality single crystals of **1–4** were sought out and sealed into capillaries to collect data. Diffraction intensity data
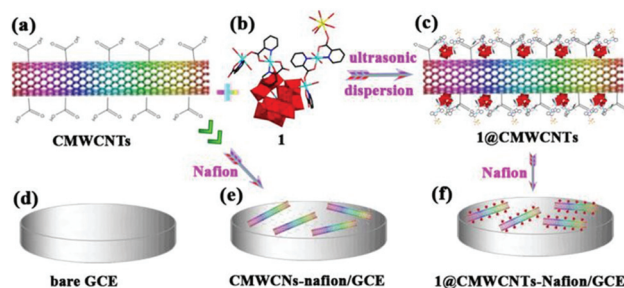

Fig. 1   The schematic preparation process of the **1**@CMWCNT–Nafion/ GCE electrochemical sensor. (a) CMWCNTs, (b) **1**, (c) **1**@CMWCNTs. (d) Bare/GCE, (e) CMWCNT–Nafion/GCE, and (f) **1**@CMWCNT–Nafion/GCE.

for **1–4** were collected on a Bruker APEX–II CCD detector at 296(2) K with graphite monochromated Mo Kα radiation ($\lambda = 0.71073$ Å). Their structures were determined by direct methods and refined F^2 by the full-matrix least-squares method using the SHELXTL–97 program package.[16] The remaining atoms were found from successive full-matrix least-squares refinements on F^2 and Fourier syntheses. Lorentz polarization and SADABS corrections were applied. All hydrogen atoms attached to carbon and nitrogen atoms were geometrically placed and refined isotropically as a riding model using the default SHELXTL parameters. No hydrogen atoms associated with water molecules were located from the difference Fourier map. All non-hydrogen atoms were refined anisotropically. The crystallographic data and structure refinements for **1–4** are reported in Table 1. Crystallographic data for **1–4** reported in this paper have been deposited in the Cambridge Crystallographic Data Centre with CCDC 1891064–1891067 for **1–4**.†
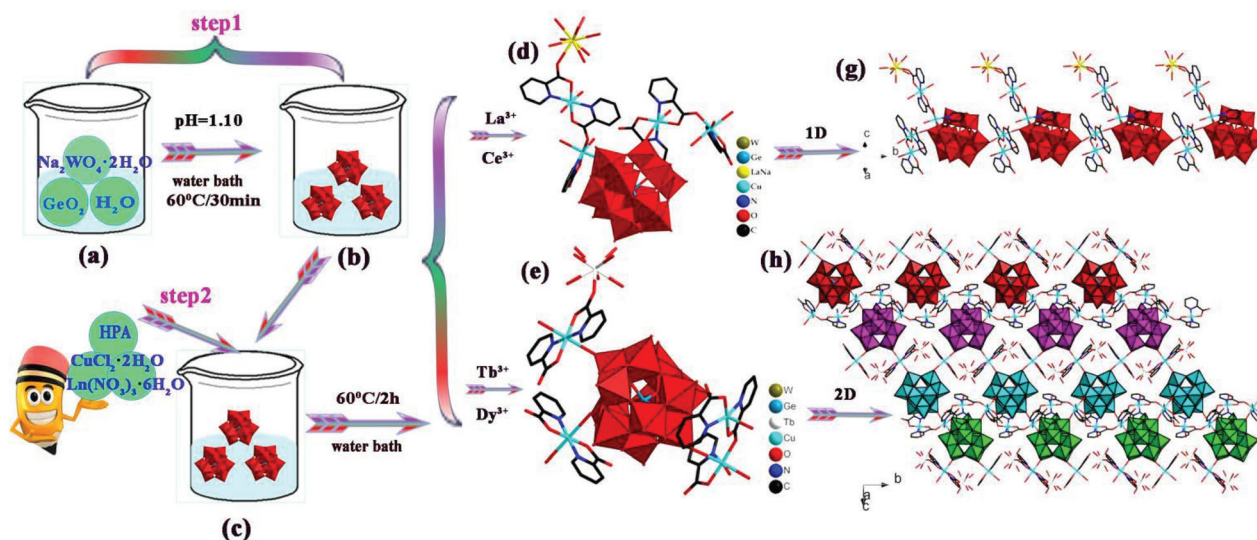
Results and discussion

Synthesis

In the past several decades, there have been many reported organic–inorganic hybrid lacunary Keggin-type DFHIPs; however, studies on organic–inorganic hybrid saturated Keggin-type DFHIPs are in their infancy; most of them just contain 3d- or 4f-metal ions. The main cause is that the lacunary POMs are easier than the saturated ones to provide vacancy sites to capture extraneous components, which brings challenges to our study. As a result, the elaborate design and preparation of novel plenary Keggin-type DFHIPs remain a great challenge. In order to overcome these difficulties, we selected the simple materials such as GeO_2 and $Na_2WO_4 \cdot 2H_2O$ with Cu^{2+} and Ln^{3+} cations to prepare Keggin-type DFHIPs in the presence of HPA under aqueous solution conditions. Herein, in the synthesis process, we chose a strategy of combining *in situ* assembly and stepwise synthesis (Fig. 2). We used sodium tungstate and GeO_2 as the initial materials, controlled the molar ratio of the reactants and adjusted the pH of the solution to construct saturated Keggin-type polyanions. Then, Cu^{2+} and Ln^{3+} cations and the carboxylic acid ligand were simultaneously introduced to synthesize novel plenary Keggin-type DFHIPs. Firstly, GeO_2 and $Na_2WO_4 \cdot 2H_2O$ and H_2O were added into a beaker, the pH value of the solution was adjusted to 1.10, and then the solution was heated in the 60 °C water bath for 0.5 h, giving rise to plenary Keggin-type $[\alpha\text{-}GeW_{12}O_{40}]^{4-}$ polyanions in this process followed by the successive addition of $CuCl_2 \cdot 2H_2O$, HPA and $Ln(NO_3)_3 \cdot 6H_2O$ into this solution. The resulting solution was kept at 60 °C for another 2 h, and cooled to room temperature and organic–inorganic hybrid plenary Keggin-type DFHIPs **1–2** and **3–4** were obtained. In addition, if the Cu^{2+} ion was replaced by other 3d-metal cations (such as Mn^{2+}, Co^{2+}, and Ni^{2+} ions) under similar conditions, no target products were acquired but just precipitates. We think that the Jahn–Teller distortion effect of the Cu^{2+} ion can favour constructing the extended structures. It is well known to us that Ln^{3+} cations have high oxophilicity

Table 1 X-ray diffraction crystallographic data and structure refinements for **1–4**

	1	2	3	4
Empirical formula	$C_{36}H_{64}Cu_4GeLa_{0.5}N_6Na_{0.5}O_{72}W_{12}$	$C_{36}H_{64}Cu_4GeCe_{0.5}N_6Na_{0.5}O_{72}W_{12}$	$C_{30}H_{52}Cu_3GeN_5O_{66}TbW_{12}$	$C_{30}H_{52}Cu_3DyGeN_5O_{66}W_{12}$
Formula weight	4346.83	4347.44	4167.10	4170.68
Crystal system	Monoclinic	Monoclinic	Monoclinic	Monoclinic
Space group	$P2_1/n$	$P2_1/n$	$P2_1/c$	$P2_1/c$
a, Å	18.7617(9)	18.7986(7)	13.2757(5)	13.241(4)
b, Å	14.7533(7)	14.7548(4)	16.5995(6)	16.539(4)
c, Å	31.1104(15)	31.1802(12)	35.2571(13)	35.111(9)
α, °	90	90	90	90
β, °	94.9910(10)	95.0180(10)	100.0500(10)	100.086(4)
γ, °	90	90	90	90
V, Å^{-3}	8578.6(7)	8615.3(5)	7650.4(5)	7570(3)
Z	4	4	4	4
μ, mm^{-1}	17.694	17.635	20.189	20.455
$F(000)$	7872	7874	7468	7472
D_c, g cm^{-3}	3.366	3.352	3.618	3.659
T, K	296(2)	296(2)	296(2)	296(2)
Limiting indices	$-19 \leq h \leq 22$	$-22 \leq h \leq 22$	$-15 \leq h \leq 15$	$-15 \leq h \leq 15$
	$-17 \leq k \leq 17$	$-17 \leq k \leq 17$	$-18 \leq k \leq 19$	$-12 \leq k \leq 19$
	$-24 \leq l \leq 36$	$-37 \leq l \leq 37$	$-41 \leq l \leq 33$	$-41 \leq l \leq 40$
Reflections collected/unique	43 205/15 057	74 790/15 104	37 659/13 226	37 973/13 124
R_{int}	0.0536	0.0358	0.0749	0.0788
Data/restrains/parameters	15 057/20/1085	15 104/2/1085	13 226/49/1023	13 124/61/1024
GOF on F^2	1.078	1.083	1.016	1.041
R_1, wR_2 $(I > 2\sigma(I))$	0.0502, 0.1095	0.0540, 0.1356	0.0610, 0.1547	0.0498, 0.1037
R_1, wR_2 (all data)	0.0709, 0.1159	0.0588, 0.1378	0.0847, 0.1666	0.0830, 0.1127

Fig. 2 (a) The solution formed by GeO_2, $Na_2WO_4 \cdot 2H_2O$ and H_2O. (b) The *in situ* generated $[\alpha\text{-}GeW_{12}O_{40}]^{4-}$ polyanions. (c) Introducing HPA, Cu^{2+} and Ln^{3+} cations to the reaction system containing *in situ* generated $[\alpha\text{-}GeW_{12}O_{40}]^{4-}$ polyanions. (d) The molecular structural unit of **1** or **2**. (e) The molecular structural unit of **3** or **4**. (f) The 1-D chain alignment of **1** or **2**. (g) The 2-D layer structure of **3** or **4**.

and a high diversity coordination number. However, when the Ln^{3+} ions meet with GT fragments in the aqueous system, precipitation is usually obtained immediately rather than crystals, the reason for which is that the direct combination between the oxyphilic Ln^{3+} cations and the oxygen-rich GT fragments easily leads to ordinary chemical precipitation. In order to resolve the difficulty, carboxylic acid ligands are introduced to participate in the reaction, which can coordinate to Ln^{3+} cations and to some extent reduce the direct combination between GT fragments and Ln^{3+} cations, which is favorable to reduce precipitation and thus HPA was chosen in our system so that it can be deprotonated by coordination to 3d- and/or 4f-metal ions. What's more, the carboxylate group can rotate in a limited way and the pyridine ring can also provide N-donor atoms; thus HPA may connect metal ions in different directions. The structural discrepancies of **1–2** and **3–4** may mainly stem from the synergistic effect between different coordinate geometries of the Ln^{3+} cations and various coordination modes of the PA⁻ ligand (Fig. S2†) because their synthetic conditions are the same. The pH effect was investigated by parallel experiments. It should be noted the pH values between 1.10 and 1.50 were optimal to the syntheses of **1–4** and their yields are the highest at pH = 1.10. When the pH is higher than 1.50 or 1.10, some amorphous precipitates were obtained. In addition, the effect of reaction temperature also cannot be ignored in the synthesis of these compounds. We can find out that the optimal reaction temperature is about 60 °C. There were no crystals in the solution at lower temperature, such as room temperature. When the temperature was raised to 100 °C or more, a few crystals were obtained with poor quality. In the future, on the one hand, we hope to obtain much more complicated DFHIPs with special properties and structures by adjusting the molar ratios of the initial materials or introdu-

cing other nitrogen-bearing polycarboxylic ligands or chiral organic ligands. On the other hand, new methods of reaction will be explored continuously, such as the hydrothermal method, microwave heating method and so on.

Structural description

Bond valence sum (BVS) calculations of **1–4** show that the oxidation states of all W, Ge, Cu and Ln elements are +6, +4, +2 and +3, respectively (Table S1†). The experimental PXRD patterns of **1–4** are in good correspondence with the simulated PXRD patterns from the single-crystal X-ray diffraction, suggesting the good phase purity of the samples (Fig. S3†). Table 1 illustrates crystal data and structural refinements of **1–4**. It should be pointed out that the crystal structures of **1–4** possess a plenary Keggin $[\alpha\text{-}GeW_{12}O_{40}]^{4-}$ polyanion. The plenary $[\alpha\text{-}GeW_{12}O_{40}]^{4-}$ polyanion belongs to the typical α-Keggin-type building block, which is composed of a GeO_4 tetrahedron at the centre surrounded by four vertex-sharing $\{W_3O_{13}\}$ trimers. Every $\{W_3O_{13}\}$ group is made up of three WO_6 octahedra linked in a triangular arrangement by sharing edges.[17] The Ge–O distances fall in the range of 1.707(9)–1.750 (11) Å and the W–O bond lengths are between 1.680(10) and 2.330(10) Å, which are all in the usual range. Single-crystal X-ray diffraction analysis indicates that **1–2** are isomorphous and crystallize in the monoclinic space group $P2_1/n$, while **3–4** are isomorphic and crystallize in the monoclinic space group $P2_1/c$. As a consequence, only the structures of **1** and **3** are representatively depicted in here. The molecular structural unit of **1** is composed of a plenary α-Keggin $[\alpha\text{-}GeW_{12}O_{40}]^{4-}$ polyanion, a peculiar bridging di-copper $[Cu_2(H_2O)_3(PA)_3]^+$ subunit and one inorganic–organic hybrid heterometal $[La_{0.5}Na_{0.5}Cu_2(H_2O)_{12}(PA)_3]^{3+}$ moiety and five lattice water molecules (Fig. 3a). More fascinatingly, in **1**, PA⁻ ligands
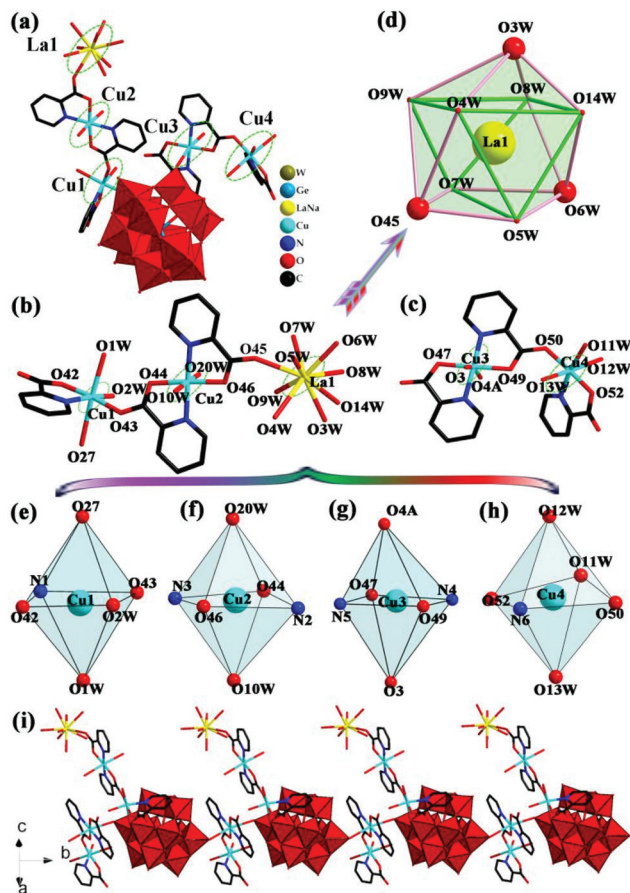
Fig. 3 (a) The molecular structural unit of **1**. (b) The bridging heterometal $[La_{0.5}Na_{0.5}Cu_2(H_2O)_{12}(PA)_3]^{3+}$ subunit in **1**. (c) The bridging di-copper $[Cu_2(H_2O)_3(PA)_3]^+$ subunit in **1**. (d) The tricapped trigonal prism geometry of the $La1^{3+}$ ion in **1**. (e) The octahedral coordination environment of the $Cu1^{2+}$ cation. (f) The octahedral geometry of the $Cu2^{2+}$ cation. (g) The octahedral coordination environment of the $Cu3^{2+}$ cation. (h) The octahedral geometry of the $Cu4^{2+}$ cation. (i) The 1-D chain alignment of **1** viewed. (La/Na: yellow; W: prasinous; Ge: blue; Cu: sky blue; O: red; N: dark blue; C: black.) Symmetry codes: A: x, −1 + y, z.

possess two different coordination modes: (1) one serves as a tridentate ligand bridging two Cu^{2+} ions through two carboxylic O atoms and a pyridine N atom or as a tridentate ligand to chelate a Cu^{2+} ion and a La^{3+} ion through two carboxylic O atoms and a pyridine N atom. (2) The other acts as a bidentate ligand chelating a Cu^{2+} ion using a carboxylic O atom and a pyridine N atom. In the heterometal $[La_{0.5}Na_{0.5}Cu_2(H_2O)_{12}(PA)_3]^{3+}$ moiety, the La1 position is simultaneously occupied by 50% $La1^{3+}$ and 50% $Na1^+$ ions, and the $[La_{0.5}Na_{0.5}(H_2O)_8]^{2+}$ cation attaches to the $\{[Cu1(H_2O)_2(PA)][Cu2(H_2O)_2(PA)_2]\}^+$ fragment *via* a carboxylic oxygen (O45) atom. The bridging di-copper $\{[Cu1(H_2O)_2(PA)][Cu2(H_2O)_2(PA)_2]\}^+$ fragment encompasses one $[Cu1(H_2O)_2(PA)]^+$ cation and one $[Cu2(H_2O)_2(PA)_2]$ subunit linked through two bridging carboxylic oxygen (O43, O44) atoms. The $[Cu1(H_2O)_2(PA)]^+$ cation includes one $Cu1^{2+}$ ion, one PA$^-$ ligand and two water molecules. Nevertheless, the $[Cu2(H_2O)_2(PA)_2]$ subunit consists of a

$Cu2^{2+}$ ion, two PA$^-$ ligands and two water molecules (Fig. 3b). On the other hand, the bridging di-copper $[Cu_2(H_2O)_3(PA)_3]^+$ subunit is made up of a $[Cu3(PA)_2]$ group and a $[Cu4(H_2O)_3(PA)]^+$ cation connected by two bridging carboxylic oxygen (O49, O50) atoms from a PA$^-$ ligand. One minor difference of the $[Cu_3(PA)_2]$ subunit with the $[Cu_2(H_2O)_2(PA)_2]$ subunit is that the Cu_3^{2+} ion coordinates with two oxygen atoms from two adjacent $[\alpha\text{-}GeW_{12}O_{40}]^{4-}$ polyanions, whereas the Cu_2^{2+} cation coordinates with two oxygen atoms from water molecules. The $[Cu4(H_2O)_3(PA)]^+$ cation is also defined by one $Cu4^{2+}$ ion, one PA$^-$ ligand and three water molecules. Similarly, one minor difference between the $[Cu4(H_2O)_3(PA)]^+$ cation and the $\{[Cu1(H_2O)_2(PA)]\}^+$ cation is that the $Cu4^{2+}$ cation has three coordination water molecules, whereas the $Cu1^{2+}$ cation has two coordination water molecules (Fig. 3c). In addition, the crystallographically independent $La1^{3+}$ ion in **1** resides in the nine-coordinate distorted tricapped trigonal prism geometry established by one carboxylic oxygen atom (O45) from a PA$^-$ ligand [La–O: 2.624(18) Å] and eight coordinate water oxygen atoms [La–O: 2.469(19)–2.808(9) Å]. In the coordination polyhedron around the $La1^{3+}$ ion in **1**, the O7W, O8W and O9W group and the O4W, O5W and O14W group constitute two bottom planes of the trigonal prism. Furthermore, O45, O3W and O6W respectively occupy three cap positions over the side planes defined by the O4W, O5W, O7W and O9W group, the O4W, O8W, O9W and O14W group and the O5W, O7W, O8W and O14W group (Fig. 3d). Interestingly, four crystallographically unique octahedral Cu^{2+} ions ($Cu1^{2+}$, $Cu2^{2+}$, $Cu3^{2+}$ and $Cu4^{2+}$) in **1** reveal four kinds of coordination environments. The $Cu1^{2+}$ ion is coordinated with one N (N1) and two O atoms (O42, O43) from two PA$^-$ ligands with Cu–N and Cu–O bond lengths in the range of 1.966(14) and 1.954(10)–1.957(11) Å, respectively, and one water O atom (O2W) [1.980(11) Å] forming the equatorial plane and another two O atoms (O27, O1W) from one adjacent $[\alpha\text{-}GeW_{12}O_{40}]^{4-}$ polyanion located at two axial vertexes with the Cu–O distance of 2.579(97) Å and one water molecule with the Cu–O distance of 2.288(15) Å (Fig. 3e). The elongated octahedral geometry of the $Cu2^{2+}$ ion (Fig. 3f) is constituted by two N (N2, N3) and two O (O44, O46) atoms from two PA$^-$ ligands [Cu–N: 1.955(15)–1.966(15) Å], [Cu–O: 1.983(13)–2.035(11) Å] in the equatorial plane and two water molecules (O20W, O10W) occupying two axial vertexes [Cu2–O: 2.448(19)–2.500(14) Å]. The elongated octahedral geometry of the $Cu3^{2+}$ ion (Fig. 3g) is made up of two N (N4, N5) and two O (O47, O49) atoms in the equatorial plane from two PA$^-$ ligands with the Cu–N and Cu–O bond lengths in the range of 1.963(14)–1.976(13) and 1.904(13)–1.981(12) Å, respectively, and two O atoms in two axial vertexes (O4A, O3) from two adjacent $[\alpha\text{-}GeW_{12}O_{40}]^{4-}$ clusters with the Cu–O distance of 2.631(11)–2.693(93) Å. The octahedral coordination sphere of the $Cu4^{2+}$ ion (Fig. 3h) is defined by one N (N6) [Cu–N: 1.996(14) Å] and two O atoms (O50, O52) [Cu–O: 1.938(12)–1.944(15) Å] from two PA$^-$ ligands, and one water ligand (O11W) [Cu–O: 2.054(19) Å] in the equatorial plane and another two water ligands (O12W, O13W) [Cu–O: 2.440(18)–2.502(22) Å] standing on two axial ver-

texes. More strikingly, the most outstanding structural feature of **1** is that neighboring molecular structural units are connected together by means of the bridging di-copper $[Cu_2(H_2O)_3(PA)_3]^+$ subunits, giving rise to a 1-D chain alignment (Fig. 3i). It should be pointed out that **1** represents the first example of an infinite 1-D chain architecture constituted by heterometal $\{[La_{0.5}Na_{0.5}Cu_2(H_2O)_{12}(PA)_3][\alpha\text{-}GeW_{12}O_{40}]\}^-$ cores and the di-copper $[Cu_2(H_2O)_3(PA)_3]^+$ linkers.

It is worth mentioning that the space packing of molecular structural units of **1** is quite interesting. In the *ab* plane, the 1-D chain alignments show the −ABAB− orderly fashion along the *a* axis (Fig. 4a and b). What's more, in the 3-D packing architecture of **1** (Fig. 4c), neighbouring 1-D chains in the lattice of **1** are arranged in the staggered fashion and further stacked in parallel along the *c* axis to give an organized −ABAB− array, which to some extent enhances the structure stability. The unambiguous arrangement mode of repeating units in layer A is shown in Fig. 4d and e, two types of spatial orientations (named line A and line A′) are tidily arranged in the −AA′AA′− fashion along the *c* axis (Fig. 4d and e). In addition, in the *bc* plane, another repeating unit in layer B that also exhibits two types of spatial orientations (named line B and line B′) are tidily arranged in the −BB′BB′− pattern along the *c* axis (Fig. 4f and g).

The molecular structural unit of **3** is composed of a plenary α-Keggin $[\alpha\text{-}GeW_{12}O_{40}]^{4-}$ polyanion, a di-copper $[Cu_2(H_2O)_2(PA)_3]^+$ subunit, 0.5 bridging $[Cu(PA)_2]$ units and one unique inorganic–organic hybrid heterobimetallic $\{Tb(H_2O)_7[Cu(PA)_2]_{0.5}\}^{3+}$ moiety and seven lattice water molecules (Fig. 5a). More fascinatingly, in **3**, PA⁻ ligands possess two different coordination modes, which is similar to **1**. In addition, in the heterobimetallic $\{Tb(H_2O)_7[Cu(PA)_2]_{0.5}\}^{3+}$ moiety, the $[Tb(H_2O)_7]^{3+}$ ion attaches

to the $\{[Cu1(PA)_2]_{0.5}\}$ group *via* two carboxylic oxygen (O31, O38) (Fig. 5b) atoms. The centrosymmetric $[Cu1(PA)_2]$ group consists of a Cu1²⁺ ion and two PA⁻ ligands. The asymmetric di-copper $[Cu_2(PA)_2(PA)_3]^+$ subunit is made up of a centrosymmetric $[Cu2(PA)_2]$ group and a $[Cu3(H_2O)_3(PA)]^+$ cation which are linked by two carboxylic oxygen (O26, O29) (Fig. 5c) atoms. Besides, the bridging $[Cu4(PA)_2]$ group is made up of a Cu4²⁺ ion and two PA⁻ ligands (Fig. 5d). Interestingly, four crystallographically unique Cu²⁺ ions (Cu1²⁺, Cu2²⁺, Cu3²⁺ and Cu4²⁺) in **3** reveal four kinds of coordination environments. Three of them (Cu1²⁺, Cu3²⁺, Cu4²⁺) display hexa-coordinate octahedral geometry, and another one exhibits a penta-coordinate square pyramid sphere. In the octahedral geometry of the Cu1²⁺ ion (Fig. 5e), two N (N1, N1A) and two oxygen (O31, O31A) atoms from two PA⁻ ligands [Cu–N: 1.983(16)–1.983(16) Å, Cu–O: 1.960(13)–1.960(13) Å] build the equatorial plane and two O atoms (O9, O9A) from two adjacent $[\alpha\text{-}GeW_{12}O_{40}]^{4-}$ polyanions [Cu–O: 2.488(13)–2.488(13) Å] stand on two polar positions. It is worth mentioning that the Cu2²⁺ ion displays a square pyramid (Fig. 5f), in which two N (N2, N3) and two O (O26, O47) atoms from two PA⁻ ligands establish the basal plane [Cu–N: 1.910(2)–1.981(16) Å, Cu–O: 1.922(14)–1.986(12) Å] and a water molecule (O8W) occupies the apical position [Cu–O: 2.350(16) Å]. In the octahedral geometry of the Cu3²⁺ ion (Fig. 5g), one N (N4) and two O atoms (O29, O53) from two PA⁻ ligands [Cu–N: 1.958(15) Å, Cu–O: 1.951(12)–1.944(14) Å] and one water molecule (O9W) [Cu–O: 1.984(14)] form the equatorial plane and another two O atoms (O15, O34B) from two adjacent $[\alpha\text{-}GeW_{12}O_{40}]^{4-}$ polyanions [Cu–O: 2.488(13)–2.547(13) Å] inhabit two axial vertexes. The octahedral coordination sphere of the Cu4²⁺ ion (Fig. 5h) is constructed from two N (N5, N5C) and two O atoms (O45, O45C) from two PA⁻

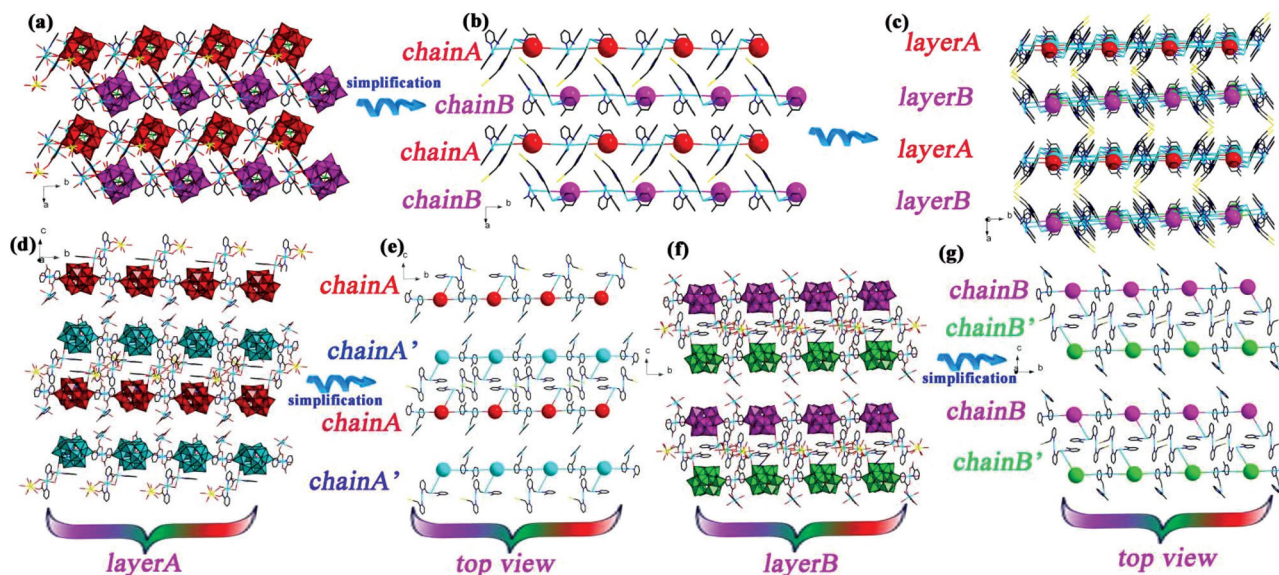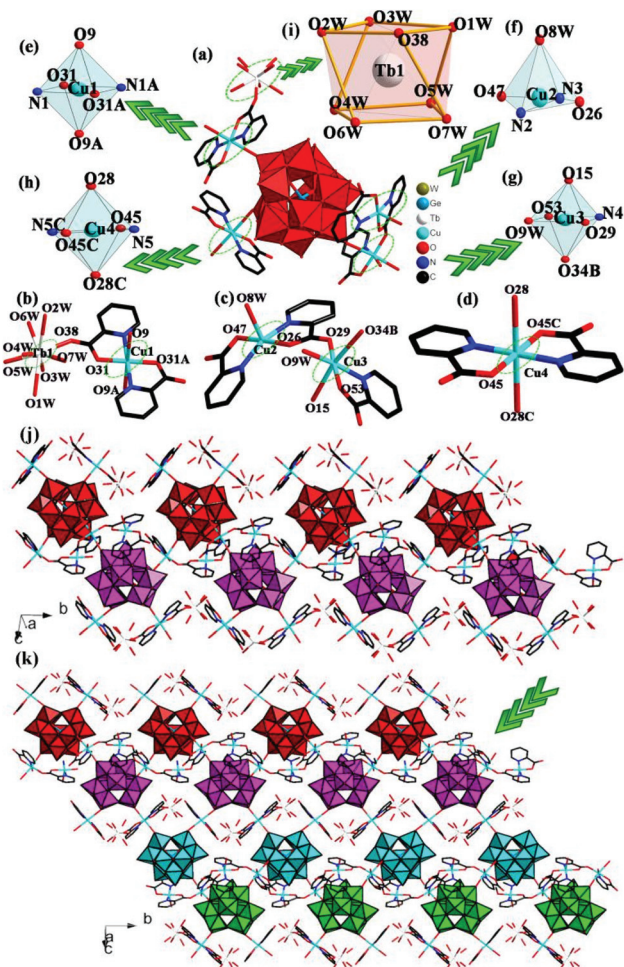**Fig. 4** (a–b) Two types of spatial orientations for polyanions in **1** in the *ab* plane. (c) The 3-D packing architecture with an organized −ABAB− array in **1** viewed along the *c* axis. (d and e) The 2-D layer (layer A) with two types of spatial orientations for polyanions in **1** along the *c* axis. (f and g) The 2-D layer (layer B) with two types of spatial orientations for polyanions in **1** along the *c* axis.

Fig. 5 (a) The molecular structural unit of **3**. (Tb: white; W: light green; Ge: blue; Cu: sky blue; O: red; N: dark blue; C: black.) (b) The bridging $[Tb(H_2O)_7Cu(PA)_2]^{3+}$ moiety in **3**. (c) The bridging $[Cu_2(H_2O)_3(PA)_3]^+$ moiety in **3**. (d) The pendent $[Cu(PA)_2]$ group in **3**. (e) The octahedral coordination environment of the $Cu1^{2+}$ cation. (f) The square pyramid geometry of the $Cu2^{2+}$ cation. (g) The octahedral geometry of the $Cu3^{2+}$ cation. (h) The octahedral geometry of the $Cu4^{2+}$ cation. (i) The view of the square antiprism geometry of the Tb^{3+} cation. (j) The view of the 1-D zigzag chain along $Cu2^{2+}$ and $Cu3^{2+}$. (k) The 2-D layer structure of **3**. Symmetry codes: A: $2 - x$, $2 - y$, $1 - z$. B: $1 - x$, $0.5 + y$, $0.5 - z$. C: $2 - x$, $3 - y$, $1 - z$.

ligands [Cu–N: 1.975(15)–1.975(15) Å, Cu–O: 1.950(13)–1.950(13) Å] and two O atoms (O28, O28C) from two adjacent $[\alpha\text{-}GeW_{12}O_{40}]^{4-}$ polyanions [Cu–O: 2.577(13)–2.577(13) Å]. In **3**, there is one crystallographically unique $Tb1^{3+}$ ion, which adopts the distorted square antiprism geometry established by one carboxylic oxygen atom (O38) from a PA^- ligand [Tb–O: 2.366(14) Å] and seven coordinate water ligands [Tb–O: 2.280(3)–2.480(15) Å] (Fig. 5i). In the coordination polyhedron around the $Tb1^{3+}$ ion in **3**, the O3W, O1W, O2W and O38 group and the O4W, O5W, O6W, and O7W group constitute two bottom planes of the distorted square antiprism geometry.

Most attractively, the most outstanding structural feature of **3** is that neighboring molecular structural units are interconnected together by virtue of the bimetallic bridging $[Cu_2(H_2O)_3(PA)_3]^+$ subunits, generating a charming zigzag 1-D chain alignment (Fig. 5j). Adjacent zigzag 1-D chains are combined with each other by heterobimetallic bridging $\{Tb(H_2O)_7[Cu(PA)_2]_{0.5}\}^{3+}$ subunits and $[Cu(PA)_2]$ groups, propagating a fascinating 2-D sheet structure (Fig. 5k). Ulteriorly, in the *bc* plane, the 2-D sheet alignments show the –ABAB– pattern viewed along the *a* axis (Fig. 6a and b), which may contribute to reduce the steric hindrance. However, in the *ac* plane, the 2-D layers are stacked in a staggered fashion with the –AAA– mode viewed along the *b* axis (Fig. 6c and d).

Electrochemical sensing properties of the 1/3@CMWCNT–Nafion/GCE electrochemical sensors towards the detection of AC

As is known to us all, Acetaminophen (AC) is a kind of long-standing material and one of the most widely used drugs.[18] Large scale therapeutic application of AC generates the need for the detection of AC with fast, simple and sensitive methodologies. Meanwhile, the electrochemical method has been used most widely for the determination of AC to date because of the high sensitivity and simplicity of this approach.[19] Recently, film modified electrodes were frequently used as the working electrodes to enhance the electric signals of substances to be determined, which attracted great attention due to their unique physical and chemical properties, just like the enhanced adsorptive ability of conducting polymer films. When it comes to this point, the selection of a suitable film-material became crucial. In addition, carbon nanotubes have caused widespread concern because of their special conductivity and their thermal, optical and machine performance and will be our first choice.[20] There are the obvious disadvantages of carbon nanotubes such as the poor dispersion in aqueous solution and spontaneous aggregation.[21] Therefore, carboxyl functionalized multi-walled carbon nanotubes (CMWCNTs) were introduced to make up for the films with good electrochemical performances, which is attributed to the larger specific surface and controlled aperture size, which can accelerate the transportation of electrolyte ions.[22] What's more, on account of the good conductivity of CMWCNTs, they can promote the electron transfer of active sites of organic molecules and the reaction rate on the surface of film modified electrodes and the reversibility of the electrochemical performances, which enable CMWCNTs to become potential chemical sensor materials.[23] Until now, some research groups have consciously dedicated great efforts to design and develop the electrode materials for the applications of electrochemistry. POM-based materials are a large family of metal–oxygen clusters with unrivalled structural diversities and intriguing physico-chemical properties and those properties enable POMs to become the ideal model platforms in various fields.[24] Our interest is focused on electrochemistry of POM-based materials, one important reason of which is that POMs can act as efficient donors or acceptors of electrons without structural change, which gives POMs ideal reversible charge transfer
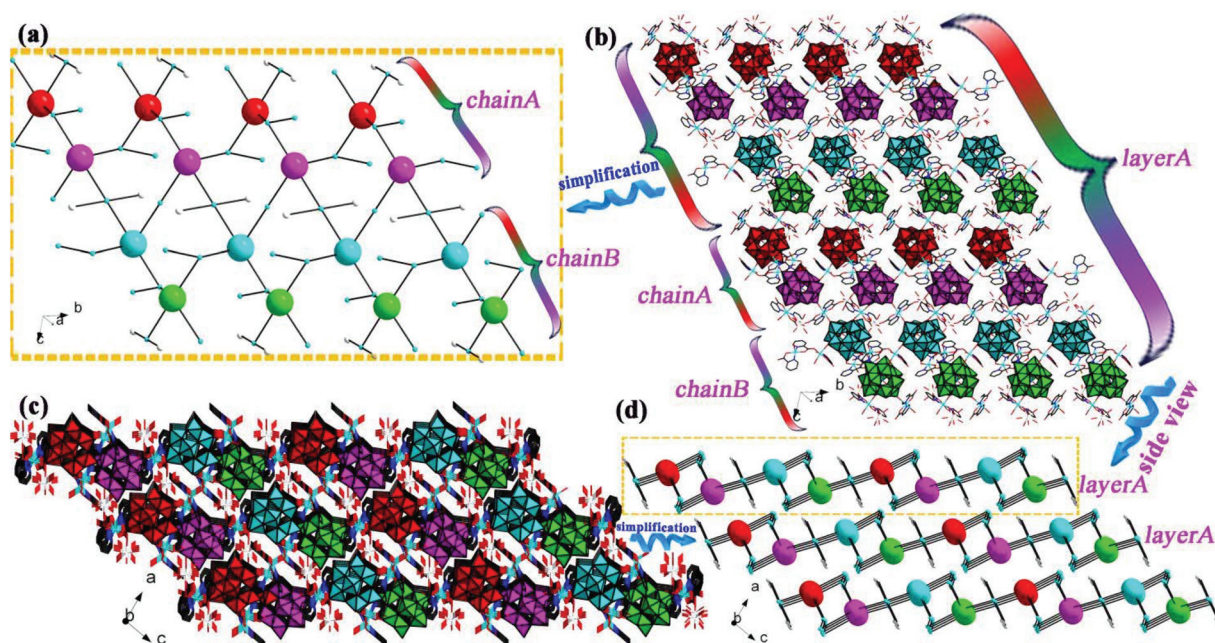
Fig. 6 (a) The simplified 2-D layer of **3** viewed along the *a* axis. (b) The 2-D layer (layer A) showing two types of spatial orientations of polyanions of **3** viewed along the *a* axis. (c) The 3-D packing of polyanions of **3** viewed along the *b* axis. (d) The simplified 3-D packing of **3** viewed along the *b* axis.

ability to serve as the candidates for electron exchange reactions.[25] Moreover, the distinct sites of POMs may provide them with certain responsive ability; therefore, POMs were chosen to be loaded on the surface of CMWCNTs to improve the conductivity and response of modified electrodes. In recent years, electrochemical applications of POMs have made major breakthroughs, although most of them used the simple POMs, such as PW_{12}, PMo_{12}, *etc.*;[26] there is no report on DFHIPs as modified electrode materials to electrochemically detect small organic drug molecules. Thus, in this paper, the as-synthesized DFHIPs **1** and **3** as the modified electrode materials were used to fabricate **1/3**@ CMWCNT–Nafion/GCE electrochemical sensors. Nafion acts as an adhesive. The electrochemical response properties of **1/3**@CMWCNT–Nafion/GCE electrochemical sensors towards the AC detection (Fig. 7 and Fig. S4–S7†) were further investigated by cyclic voltammetry in the 0.1 mol L^{-1} NaH_2PO_4–Na_2HPO_4 buffer solution (pH = 8.0).

The CV responses of the bare GCE, CMWCNT–Nafion/GCE and **1**@CMWCNT–Nafion/GCE were first examined in 50 mL of 0.1 mol L^{-1} NaH_2PO_4–Na_2HPO_4 buffer solution in the absence of AC (Fig. S4a†). As shown in Fig. S4a,† when the bare GCE was used, no redox peak was observed; when the CMWCNT–Nafion/GCE was placed into the buffer solution, a couple of weak redox waves were observed, which correspond to the redox process of carboxylic acid on the surface of CMWNTs;[27] when the CV of **1**@CMWCNT–Nafion/GCE was put in the buffer solution, moreover, three oxidation peaks at −0.430 V, 0.024 V and 0.186 V and three reduction peaks at −0.678 V, −0.422 V and −0.048 V appeared. The first two pairs

of redox waves are attributed to the redox process of W(VI) centers, while the last pair of redox waves is attributed to the redox process of Cu(II) cations. The CV responses of the bare GCE, CMWCNT–Nafion/GCE and **1**@CMWCNT–Nafion/GCE were also recorded in 50 mL 0.1 mol L^{-1} NaH_2PO_4–Na_2HPO_4 buffer solution in the presence of 1 mmol L^{-1} AC (Fig. 7a). As shown in Fig. 7a, it is apparently obvious that a very weak oxidation peak is seen at 0.42 V and a reduction peak at 0.22 V is seen using the bare GCE in the presence of AC, which can be attributed to the redox process of AC and this redox peak can be used to detect the signal of the working electrodes. Correspondingly, the CV responses of the CMWCNT–Nafion/GCE and **1**@CMWCNTs–Nafion/GCE show relatively stronger redox peaks of AC. The redox peak of AC for the **1**@CMWCNT–Nafion/GCE is the strongest and the midpoint potential of the redox peak of AC is at $E_{1/2}$ = 0.375 V. The remarkable enhancement of the redox peak signal of AC for the **1**@CMWCNTs–Nafion/GCE may be attributed to the adsorption of AC from solution to the surface of **1**@CMWCNTs–Nafion/GCE through hydrogen bonding and physical adsorption interactions between AC and **1** or CMWCNTs. The CV curve of the **1**@CMWCNTs–Nafion/GCE exhibits good reversibility of the redox process of AC on the surface of working electrodes, and also denotes that the **1**@CMWCNT–Nafion/GCE shows good sensing performance towards the AC detection and can serve as an electrochemical sensor towards the AC detection. This observation suggests that **1** plays the major role in the improvement of sensing performance of the **1**@CMWCNT–Nafion/GCE. Besides, the occurrence of characteristic redox peaks of the W^{VI} and Cu^{II} centers in the CVs of the **1**@CMWCNT–
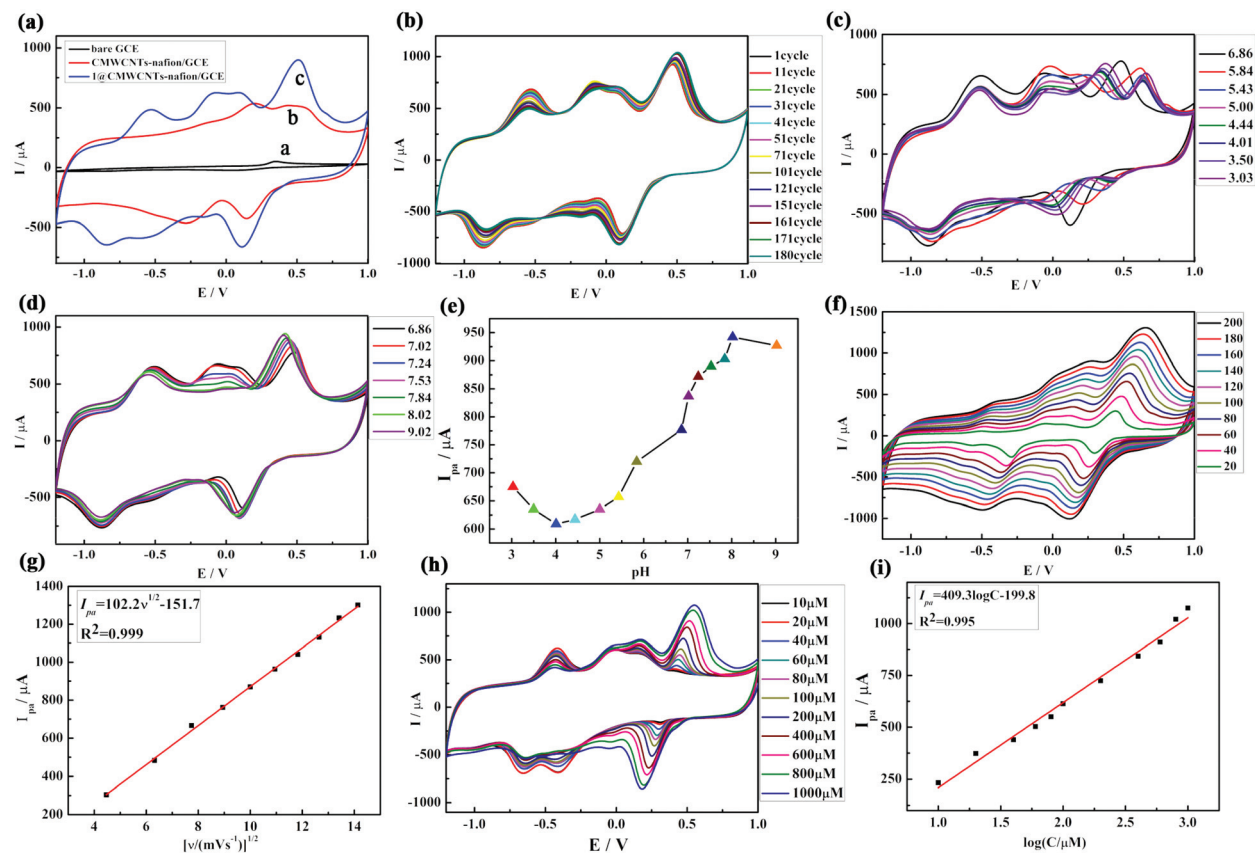
Fig. 7 (a) Comparison of CVs of the bare GCE, CMWCNT–Nafion/GCE and **1**@CMWCNT–Nafion/GCE in 0.1 mol L^{-1} NaH$_2$PO$_4$–Na$_2$HPO$_4$ buffer solution (pH = 8.0) in the presence of 1.0 mmol L^{-1} AC (scan rate: 100 mV s^{-1}). (b) CVs of the **1**@CMWCNT–Nafion/GCE electrochemical sensor from the 1st round to the 180th round in 0.1 mol L^{-1} NaH$_2$PO$_4$–Na$_2$HPO$_4$ buffer solution in the presence of 1.0 mmol L^{-1} AC (scan rate: 100 mV s^{-1}). (c) CVs of the **1**@CMWCNT–Nafion/GCE electrochemical sensor in 0.1 mol L^{-1} NaH$_2$PO$_4$–Na$_2$HPO$_4$ buffer solution in the presence of 1.0 mmol L^{-1} AC in the acidic direction (from 3.0 to 6.86). Scan rate: 100 mV s^{-1}. (d) CVs of the **1**@CMWCNT–Nafion/GCE electrochemical sensor in 0.1 mol L^{-1} NaH$_2$PO$_4$–Na$_2$HPO$_4$ buffer solution in the presence of 1.0 mmol L^{-1} AC in the alkaline direction (from 6.86 to 9.0). Scan rate: 100 mV s^{-1}. (e) The relationship of the anodic peak current of AC using the **1**@CMWCNT–Nafion/GCE electrochemical sensor with varying the pH value of the supporting electrolyte. (f) CVs of the **1**@CMWCNT–Nafion/GCE electrochemical sensor at different scan rates (from 20 to 200 mV s^{-1}) in the presence of 1.0 mmol L^{-1} AC. (g) The relationship of the anodic peak current (I_{pa}) with the square root of scan rate ($v^{1/2}$). (h) CVs of the **1**@CMWCNT–Nafion/GCE electrochemical sensor in 0.1 mol L^{-1} NaH$_2$PO$_4$–Na$_2$HPO$_4$ buffer solution (pH = 8.0) containing different concentrations of AC (from 10 to 1000 μmol L^{-1}). (i) The plot of the anodic peak current *versus* the logarithm of different concentrations of AC (10 to 1000 μmol L^{-1}).

Nafion/GCE also identifies the loading of **1** onto the **1**@CMWCNT–Nafion/GCE. The electrochemical sensing response mechanism of the **1**@CMWCNT–Nafion/GCE electrochemical sensor towards the AC detection can be hypothesized as follows: (1) there may exist hydrogen bonding and physical adsorption interactions between AC and CMWCNTs on the surface of the electrochemical sensor, which makes a non-ignorable contribution to the electrochemical response towards AC; (2) the synergistic effect between MWCNTs and DFHIPs **1** can improve the conductivity of the **1**@CMWCNT–Nafion/GCE electrochemical sensor;[22,26a] (3) the π–π interactions between AC molecules and PA ligands on DFHIPs **1** can also promote the electrochemical response ability of the **1**@CMWCNT–Nafion/GCE electrochemical sensor.[28]

The stability of the **1**@CMWCNT–Nafion/GCE electrochemical sensor was examined in 0.1 mol L^{-1} NaH$_2$PO$_4$–Na$_2$HPO$_4$ buffer solution in the presence of 1.0 mmol L^{-1} AC

(pH = 8.0, C_{AC} = 1.0 mmol L^{-1}, V = 50 mL) at a scan rate of 100 mV s^{-1} for 180 cycles (Fig. 7b). The resulting CVs almost overlap with each other and display no recession in the peak current intensity of AC, which confirms the good stability of the **1**@CMWCNT–Nafion/GCE electrochemical sensor and the reliability of these results. The unexpected stability of the **1**@CMWCNT–Nafion/GCE electrochemical sensor maybe results from the coordination interactions between the Cu^{2+} ions on **1** and carboxyl groups on CMWCNTs.

The selection of the optimal pH value was also essential to the response performance of the **1**@CMWCNT–Nafion/GCE electrochemical sensor, because of the following two reasons: on the one hand, it is well known that the redox reaction of AC can be described as the following equation: Acetaminophen = *N*-acetyl-*p*-quinoneimine + 2H$^+$ + 2e$^-$.[29] There is no doubt that the variation of the acidity and alkalinity of the supporting electrolyte will bring about inevitable influence on the redox

procedure of AC because of the involvement of protons in the overall electrode reaction. On the other hand, the stability of **1** in aqueous solution under different pH values is also a key factor and should be taken into consideration. The polyanion of **1** in aqueous solution is stable over a wide pH range (*ca.* 3.0–9.0), which is proved by UV spectra under different pH values (Fig. S5a and b†) and CV measurements under different pH values (Fig. S6a and b†). Moreover, it is noteworthy that the UV spectra of **1** almost remain unchanged at room temperature for seven days (Fig. S5c†), which preliminarily implies that **1** is relatively stable in aqueous solution for seven days. Furthermore, the influence of pH on the CVs of the **1**@CMWCNT–Nafion/GCE electrochemical sensor in 0.1 mol L^{-1} NaH$_2$PO$_4$–Na$_2$HPO$_4$ buffer solution in the absence of AC (Fig. S6c and d†) was explored at different pH values. The acidity or alkalinity of the buffer solution was adjusted by using concentrated phosphoric acid and 2.0 mol L^{-1} NaOH solution. Research results demonstrate the pH stable range of the **1**@CMWCNT–Nafion/GCE electrochemical sensor in 0.1 mol L^{-1} NaH$_2$PO$_4$–Na$_2$HPO$_4$ buffer solution is *ca.* 3.0–9.0 (Fig. S6c and d†). Then the electrochemical response signals of the **1**@CMWCNT–Nafion/GCE electrochemical sensor in 0.1 mol L^{-1} NaH$_2$PO$_4$–Na$_2$HPO$_4$ buffer solution in the presence of 1.0 mmol L^{-1} AC in the pH range of *ca.* 3.0–9.0 were measured (Fig. 7c and d). It can be observed from Fig. 7e that upon the increase of the pH value of the supporting electrolyte in the range of *ca.* 3.0–9.0, the intensity of the anodic peak current of AC firstly decreases until *ca.* pH = 4.0, then quickly increases and reaches the maximum at *ca.* pH = 8.0, and finally gradually declines. Hence, pH = 8.0 was applied as the optimal pH value used for evaluating the sensing performance of the **1**@CMWCNT–Nafion/GCE electrochemical sensor towards the detection of AC.

The effect of the scan rate (*v*) on the sensing performance of the **1**@CMWCNT–Nafion/GCE electrochemical sensor was also explored in 0.1 mol L^{-1} NaH$_2$PO$_4$–Na$_2$HPO$_4$ buffer solution in the presence of 1.0 mmol L^{-1} AC under the pH = 8 conditions in the range of 20–200 mV s^{-1} (Fig. 7f). Fig. 7g illustrates the variation of the anodic peak current (I_{pa}) of AC with the scan rate. When the scan rate varies from 20 to 200 mV s^{-1}, the anodic peak current (I_{pa}) of AC increases with the increase of the scan rate (*v*), presenting a linear relationship between the anodic peak current (I_{pa}) of AC and the square root of scan rate that can be fitted to the equation: $I_{pa}(\mu A) = 102.2 \times [v(mV\ s^{-1})]^{0.5} - 151.7$ (the correlation coefficient is $R^2 = 0.999$), suggesting a diffusion-controlled electron-transfer process occurring on the **1**@CMWCNT–Nafion/GCE. Meanwhile, ΔE_p (the separation between anodic and cathodic peak potentials of AC) increased slowly with increasing scan rate, which could be attributed to the limitation associated with charge transfer on the surface of the electrode.[30]

Finally, under the pH = 8.0 experimental conditions, the variation of the peak currents of AC on the **1**@CMWNT–Nafion/GCE electrochemical sensor with increasing the concentration of AC from 10 to 1000 µmol L^{-1} was investigated (Fig. 7h). It can be explicitly seen that, with the increase of the

concentration of AC, the anodic and cathodic peak currents of AC on the **1**@CMWNT–Nafion/GCE electrochemical sensor gradually increase, which demonstrates that the **1**@CMWNTs–Nafion/GCE electrochemical sensor displays the good sensing performance towards the AC detection. Moreover, the anodic peak current linearly increases with the logarithm of the AC concentration (*C* = 10 to 1000 µmol L^{-1}) and the corresponding regression equation was I_{pa} (µA) = 409.3 × log *C* (µmol L^{-1}) − 199.8 with a correlation coefficient of 0.995 (Fig. 7i). The LOD was calculated to be 1.07 µmol L^{-1} based on three times the standard deviation of the blank sample measurement with a linear concentration range of 10–1000 µmol L^{-1}.

Under similar conditions, the electrochemical sensing properties of the **3**@CMWCNT–Nafion/GCE electrochemical sensor towards the detection of AC were also examined and are shown in Fig. S7.† Experimental results show that the **3**@CMWNTs–Nafion/GCE electrochemical sensor displays good sensing performance towards the AC detection.

The LOD of the **3**@CMWNT–Nafion/GCE electrochemical sensor is 1.08 µmol L^{-1} with a linear concentration range from 10 µmol L^{-1} to 1000 µmol L^{-1}. In addition, the chemical components in the surfaces of **1**@CMWNT–Nafion/GCE or **3**@CMWNTs–Nafion/GCE have been confirmed by using an energy dispersive spectrometer (EDS) (Fig. S8†) and the results show that DFHIPs **1** or **3** are loaded onto the surfaces of the electrochemical sensor because of the existence of the signals of W, Ge, Cu and Ln elements. What's more, the C signals are mainly from CMWCNs and DFHIPs **1** or **3**. The mass percentages and atomic percentages of all the elements are provided in Table S3.† In a word, the **1/3**@CMWCNT–Nafion/GCE electrochemical sensors show good stability and high sensitivity towards the detection of AC. Such good results provide POM-based materials with potential application prospects in the electrochemical sensing field and the low LOD can also promote the electrochemical trace amount detection of POM-based materials.

Conclusions

In conclusion, two kinds of organic–inorganic hybrids **1–4** assembled from plenary Keggin-type POM units and 3d–4f heterometal clusters were prepared *via* the strategy of combining the *in situ* assembly reaction and stepwise synthesis in aqueous solution, which represent the first organic–inorganic 3d–4f heterometal plenary Keggin-type GTs. Electrochemical measurements show that the **1/3**@CMWCNT–Nafion/GCE electrochemical sensors reveal the good stability and the good sensing performance towards the AC detection. All in all, this work shows that a great deal of rational structural design in the realm of organic–inorganic hybrid plenary α-Keggin-type DFHIPs is possible and would open new opportunities for POM-based materials serving as biosensors for sensitive detection of biomolecules. A further study will be carried out by utilizing other functional multi-carboxylic ligands to synthesize

more unpredictable DFHIPs so as to exploit their electrochemical sensing applications.

Conflicts of interest

There are no conflicts to declare.

Acknowledgements

References

1 (a) I. V. Kozhevnikov, *Chem. Rev.*, 1998, **98**, 171; (b) A. Müller, F. Peters, M. T. Pope and D. Gatteschi, *Chem. Rev.*, 1998, **98**, 239; (c) J. Zhou, J. W. Zhao, Q. Wei, J. Zhang and G. Y. Yang, *J. Am. Chem. Soc.*, 2014, **136**, 5065; (d) J. C. Liu, J. Luo, Q. Han, J. Cao, L. J. Chen, Y. Song and J. W. Zhao, *J. Mater. Chem. C*, 2017, **5**, 2043; (e) E. Coronado and C. J. Gómez-García, *Chem. Rev.*, 1998, **98**, 273; (f) S. G. Mitchell, C. Streb, H. N. Miras, T. Boyd, D. L. Long and L. Cronin, *Nat. Chem.*, 2010, **2**, 308; (g) Y. F. Wang and I. A. Weinstock, *Chem. Soc. Rev.*, 2012, **41**, 7479; (h) J. W. Zhao, Y. Z. Li, L. J. Chen and G. Y. Yang, *Chem. Commun.*, 2016, **52**, 4418.

2 (a) C. Ritchie, M. Speldrich, R. W. Gable, L. Sorace, P. Kögerler and C. Boskovic, *Inorg. Chem.*, 2011, **50**, 7004; (b) C. Ritchie, V. Baslon, E. G. Moore, C. Reber and C. Boskovic, *Inorg. Chem.*, 2012, **51**, 1142; (c) K. Y. Wang, B. S. Bassil, Z. G. Lin, A. Haider, J. Cao, H. Stephan, K. Viehweger and U. Kortz, *Dalton Trans.*, 2014, **43**, 16143; (d) J. C. Liu, Q. Han, L. J. Chen, J. W. Zhao, C. Streb and Y. F. Song, *Angew. Chem., Int. Ed.*, 2018, **57**, 8416.

3 (a) Y. Y. Hu, T. T. Zhang, X. Zhang, D. C. Zhao, X. B. Cui, Q. S. Huo and J. Q. Xu, *Dalton Trans.*, 2016, **45**, 2562; (b) X. J. Kong, Z. K. Lin, Z. M. Zhang, T. Zhang and W. B. Lin, *Angew. Chem., Int. Ed.*, 2016, **55**, 6411; (c) X. Ma, H. L. Li, L. J. Chen and J. W. Zhao, *Dalton Trans.*, 2016, **45**, 4935; (d) H. L. Li, Y. J. Liu, R. Zheng, L. J. Chen, J. W. Zhao and G. Y. Yang, *Inorg. Chem.*, 2016, **55**, 3881; (e) Q. Han, J. C. Liu, Y. Wen, L. J. Chen, J. W. Zhao and G. Y. Yang, *Inorg. Chem.*, 2017, **56**, 7257; (f) X. Ma, W. Yang, L. J. Chen and J. W. Zhao, *CrystEngComm*, 2015, **17**, 8175; (g) Z. Li, X. X. Li, T. Yang, Z. W. Cai and S. T. Zheng, *Angew. Chem., Int. Ed.*, 2017, **56**, 2664; (h) P. T. Ma, R. Wan, Y. Y. Wang, F. Hu, D. D. Zhang, J. Y. Niu and J. P. Wang, *Inorg. Chem.*, 2016, **55**, 918.

4 H. Miao, X. Xu, W. W. Ju, H. X. Wan, Y. Zhang, D. R. Zhu and Y. Xu, *Inorg. Chem.*, 2014, **53**, 2757.

5 (a) L. J. Chen, F. Zhang, X. Ma, J. Luo and J. W. Zhao, *Dalton Trans.*, 2015, **44**, 12598; (b) R. Gupta, F. Hussain, M. Sadakane, C. Kato, K. Inoue and S. Nishihara, *Inorg. Chem.*, 2016, **55**, 8292; (c) H. Y. Zhao, J. W. Zhao, B. F. Yang, H. He and G. Y. Yang, *CrystEngComm*, 2013, **15**, 8186; (d) Y. H. Chen, L. H. Sun, S. Z. Chang, L. J. Chen and J. W. Zhao, *Inorg. Chem.*, 2018, **57**, 15079.

6 J. F. Cao, S. X. Liu, R. G. Cao, L. H. Xie, Y. H. Ren, C. Y. Gao and L. Xu, *Dalton Trans.*, 2008, 115.

7 B. Nohra, P. Mialane, A. Dolbecq, E. Rivière, J. Marrot and F. Sécheresse, *Chem. Commun.*, 2009, 2703.

8 J. Y. Niu, S. W. Zhang, H. N. Chen, J. W. Zhao, P. T. Ma and J. P. Wang, *Cryst. Growth Des.*, 2011, **11**, 3769.

9 H. Y. Zhao, J. W. Zhao, B. F. Yang, H. He and G. Y. Yang, *Cryst. Growth Des.*, 2013, **13**, 5169.

10 J. W. Zhao, J. Cao, Y. Z. Li, J. Zhang and L. J. Chen, *Cryst. Growth Des.*, 2014, **14**, 6217.

11 J. Cai, X. Y. Zheng, J. Xie, Z. H. Yan, X. J. Kong, Y. P. Ren, L. S. Long and L. S. Zheng, *Inorg. Chem.*, 2017, **56**, 8439.

12 Y. N. Gu, Y. Chen, Y. L. Wu, S. T. Zheng and X. X. Li, *Inorg. Chem.*, 2018, **57**, 2472.

13 (a) J. Wang, J. W. Zhao, H. Y. Zhao, B. F. Yang, H. He and G. Y. Yang, *CrystEngComm*, 2014, **16**, 252; (b) J. W. Zhao, D. Y. Shi, L. J. Chen, Y. Z. Li, P. T. Ma, J. P. Wang and J. Y. Niu, *Dalton Trans.*, 2012, **41**, 10740; (c) J. W. Zhao, Y. Z. Li, F. Ji, J. Yuan, L. J. Chen and G. Y. Yang, *Dalton Trans.*, 2014, **43**, 5694; (d) J. W. Zhao, D. Y. Shi, L. J. Chen, P. T. Ma, J. P. Wang, J. Zhang and J. Y. Niu, *Cryst. Growth Des.*, 2013, **13**, 4368; (e) S. Reinoso and J. R. Galán-Mascarós, *Inorg. Chem.*, 2010, **49**, 377; (f) S. Reinoso, J. R. Galán-Mascarós and L. Lezama, *Inorg. Chem.*, 2011, **50**, 9587; (g) M. Ibrahim, V. Mereacre, N. Leblanc, W. Wernsdorfer, C. E. Anson and A. K. Powell, *Angew. Chem., Int. Ed.*, 2015, **54**, 15574.

14 (a) B. Li, J. W. Zhao, S. T. Zheng and G. Y. Yang, *Inorg. Chem.*, 2009, **48**, 8294; (b) Y. Z. Li, J. Luo, L. J. Chen and J. W. Zhao, *RSC Adv.*, 2014, **4**, 50679.

15 (a) F. Hussain, R. W. Gable, M. Speldrich, P. Kögerler and C. Boskovic, *Chem. Commun.*, 2009, 328; (b) F. Hussain, B. Spingler, F. Conrad, M. Speldrich, P. Kögerler, C. Boskovic and G. R. Patzke, *Dalton Trans.*, 2009, 4423; (c) F. Hussain, F. Conrad and G. R. Patzke, *Angew. Chem., Int. Ed.*, 2009, **48**, 9088; (d) F. Hussain and G. R. Patzke, *CrystEngComm*, 2011, **13**, 530.

16 (a) G. M. Sheldrick, *SHELXS 97, Program for Crystal Structure Solution*, University of Göttingen, Göttingen, Germany, 1997; (b) G. M. Sheldrick, *SHELXL 97, Program for Crystal Structure Refinement*, University of Göttingen, Germany, 1997.

17 N. Wu, Y. Qin, X. L. Wang, C. Qin and E. B. Wang, *Inorg. Chem. Commun.*, 2013, **37**, 174.

18 Q. C. Chu, L. M. Jiang, X. H. Tian and J. N. Ye, *Anal. Chim. Acta*, 2008, **606**, 246.

19 (*a*) Z. A. Alothman, N. Bukhari, S. M. Wabaidur and S. Haider, *Sens. Actuators, B*, 2010, **146**, 314; (*b*) H. Y. Xiong, H. Xu, L. Wang and S. F. Wang, *Microchim. Acta*, 2009, **167**, 129; (*c*) B. Habibi, M. Jahanbakhshi and M. H. Pournaghiazar, *Microchim. Acta*, 2011, **172**, 147; (*d*) F. Ghorbani-Bidkorbeh, S. Shahrokhian, A. Mohammadi and R. Dinarvand, *Electrochim. Acta*, 2010, **55**, 2752.

20 (*a*) A. Thess, R. Lee, P. Nikolaev, H. J. Dai, P. Petit, J. Robert, C. H. Xu, Y. H. Lee, S. G. Kim, A. G. Rinzler, D. T. Colbert, G. E. Scuseria, D. Tomanek, J. E. Fischer and R. E. Smalley, *Science*, 1996, **273**, 483; (*b*) H. Naeimi, A. Mohajeri, L. Moradi and A. M. Rashidi, *Appl. Surf. Sci.*, 2009, **256**, 631.

21 (*a*) J. Talla, D. H. Zhang, M. Kandadai, A. Avadhanula and S. Curran, *Physica B*, 2010, **405**, 4570; (*b*) J. F. Shen, W. S. Huang, L. P. Wu, Y. Z. Hu and M. X. Ye, *Mater. Sci. Eng., A*, 2007, **464**, 151.

22 A. Hirsch, *Angew. Chem., Int. Ed. Engl.*, 2002, **41**, 1853.

23 (*a*) H. J. Salavagione, A. M. Díez-Pascual, E. Lázaro, S. Verab and M. A. Gómez-Fatou, *J. Mater. Chem. A*, 2014, **2**, 14289;

24 A. Dolbecq, E. Dumas, C. R. Mayer and P. Mialane, *Chem. Rev.*, 2010, **110**, 6009.

25 G. J. Zhang, B. Keita, R. N. Biboum, F. Miserque, P. Berthet, A. Dolbecq, P. Mialane, L. Catalae and L. Ndjo, *J. Mater. Chem.*, 2009, **19**, 8639.

26 (*a*) Y. F. Zhang, X. J. Bo, A. Nsabimana, A. Munyentwali, C. Han, M. Li and L. P. Guo, *Biosens. Bioelectron.*, 2015, **66**, 191; (*b*) A. K. Cuentas-Gallegos, M. Lira-Cantú, N. Casañ-Pastor and P. Gómez-Romero, *Adv. Funct. Mater.*, 2005, **15**, 1125; (*c*) P. Gómez-Romero, M. Chojak, K. Cuentas-Gallegos, J. A. Asensio, P. J. Kulesza, N. Casañ-Pastor and M. Lira-Cantú, *Electrochem. Commun.*, 2003, **5**, 149; (*d*) L. Cheng, G. E. Pacey and J. A. Cox, *Electrochim. Acta*, 2001, **46**, 4223.

27 G. C. Zhao, L. Zhang, X. W. Wei and Z. S. Yang, *Electrochem. Commun.*, 2003, **5**, 825.

28 X. H. Kang, J. Wang, H. Wu, J. Liu, I. A. Aksay and Y. H. Lin, *Talanta*, 2010, **81**, 754.

29 C. X. Xu, K. J. Huang, Y. Fan, Z. W. Wu and J. Li, *J. Mol. Liq.*, 2012, **165**, 32.

30 C. X. Xu, K. J. Huang, Y. Fan, Z. W. Wu, J. Li and T. Gan, *Mater. Sci. Eng., C*, 2012, **32**, 969.